J. Fluid Mech. (2016), *vol.* 792, *pp.* 499–525. © Cambridge University Press 2016
doi:10.1017/jfm.2016.93

The behaviour of Tollmien–Schlichting waves undergoing small-scale localised distortions

Hui Xu[1,2], Spencer J. Sherwin[1,†], Philip Hall[2] and Xuesong Wu[2]

[1]Department of Aeronautics, Imperial College, London SW7 2AZ, UK

[2]Department of Mathematics, Imperial College, London SW7 2AZ, UK

(Received 29 March 2015; revised 14 September 2015; accepted 1 February 2016;
first published online 3 March 2016)

This paper is concerned with the behaviour of Tollmien–Schlichting (TS) waves experiencing small localised distortions within an incompressible boundary layer developing over a flat plate. In particular, the distortion is produced by an isolated roughness element located at $Re_{x_c} = 440\,000$. We considered the amplification of an incoming TS wave governed by the two-dimensional linearised Navier–Stokes equations, where the base flow is obtained from the two-dimensional nonlinear Navier–Stokes equations. We compare these solutions with asymptotic analyses which assume a linearised triple-deck theory for the base flow and determine the validity of this theory in terms of the height of the small-scale humps/indentations taken into account. The height of the humps/indentations is denoted by h, which is considered to be less than or equal to $x_c Re_{x_c}^{-5/8}$ (corresponding to $h/\delta_{99} < 6\,\%$ for our choice of Re_{x_c}). The rescaled width $\hat{d}$ ($\equiv d/(x_c Re_{x_c}^{-3/8})$) of the distortion is of order $O(1)$ and the width d is shorter than the TS wavelength ($\lambda_{TS} = 11.3\delta_{99}$). We observe that, for distortions which are smaller than 0.1 of the inner deck height ($h/\delta_{99} < 0.4\,\%$), the numerical simulations confirm the asymptotic theory in the vicinity of the distortion. For larger distortions which are still within the inner deck ($0.4\,\% < h/\delta_{99} < 5.5\,\%$) and where the flow is still attached, the numerical solutions show that both humps and indentations are destabilising and deviate from the linear theory even in the vicinity of the distortion. We numerically determine the transmission coefficient which provides the relative amplification of the TS wave over the distortion as compared to the flat plate. We observe that for small distortions, $h/\delta_{99} < 5.5\,\%$, where the width of the distortion is of the order of the boundary layer, a maximum amplification of only $2\,\%$ is achieved. This amplification can however be increased as the width of the distortion is increased or if multiple distortions are present. Increasing the height of the distortion so that the flow separates ($7.2\,\% < h/\delta_{99} < 12.8\,\%$) leads to a substantial increase in the transmission coefficient of the hump up to $350\,\%$.

Key words: boundary layers, instability, Navier–Stokes equations

1. Introduction

In a flat-plate boundary layer, laminar–turbulent transition can be triggered by the growth of small-amplitude perturbations, such as Tollmien–Schlichting (TS) waves. In

† Email address for correspondence: jfluidmech@imperial.ac.uk

a low-level disturbance environment such as the flight condition at cruise altitude, the process of laminar–turbulent transition can be subdivided into three stages: receptivity, linear eigenmode growth and nonlinear breakdown to turbulence. The instability of TS waves is the second stage of this process, the mathematics for which was established nearly 80 years ago (Schlichting 1968). TS instability waves grow in accordance with linear stability theory until nonlinear and three-dimensional effects contribute to the flow breakdown to turbulence (Kachanov 1994). Since the existence of TS instability waves was confirmed by Schubauer & Skramstad (1948), there have been many studies undertaken to explore and further explain transition.

Instability and transition are influenced by a multitude of physical factors (e.g. non-parallelism, nonlinearity and external disturbances which may operate on different time and/or length scales). In order to account for their influences in a systematic manner, high-Reynolds-number asymptotic approaches have been developed. Among these, the first application of the triple-deck theory to describe the linear and nonlinear growth of lower-branch TS waves is apparently due to Smith (1979*a*,*b*) although Lin (1966) clearly recognised the appropriate large-Reynolds-number scalings for TS waves long before triple-deck theory was invented. The investigation by Smith (1979*b*) showed how non-parallel effects could be taken care of in a self-consistent manner using asymptotic methods. Previously Gaster (1974) used a successive approximation procedure to tackle the same type of problem. Subsequently Smith (1979*a*) showed how the nonlinear growth of TS waves could be taken into account using triple-deck theory. However, the results of Smith (1979*a*), and the subsequent extension to three-dimensional modes by Hall & Smith (1984), are confined to the weakly nonlinear stage where an amplitude equation in an ordinary differential equation form describes the initial stage of the bifurcation from a linearly growing disturbance. Some years later Smith & Burggraf (1985) discussed the high-frequency limit of the lower-branch triple-deck problem and uncovered nonlinear structures governing successively more nonlinear stages; related work on the high-frequency limit had been previously carried out by Zhuk & Ryzhov (1982). Moston, Stewart & Cowley (2000) showed that the nonlinearly generated mean flow may develop a singularity and discussed its implication for the realisability of these nonlinear stages.

Free-stream disturbances are related to receptivity mechanisms. Receptivity is the initial stage of the natural transition process, which consists of the transformation of environmental disturbances, such as acoustic (sound) or vorticity (turbulence), into small perturbations within the boundary layer (Morkovin 1969). Receptivity establishes the initial conditions of disturbance amplitude, frequency and phase for the breakdown of laminar flow (Morkovin 1969; Saric, Reed & Kerschen 2002). Reviews of different receptivity mechanisms are given by Nishioka & Morkovin (1986), Heinrich, Choudhari & Kerschen (1988), Goldstein & Hultgren (1989), Kerschen (1989), Kozlov & Ryzhov (1990), Choudhari & Streett (1994), Crouch (1994), Wlezien (1994), Kachanov (2000) and Saric *et al.* (2002). The early theoretical work of Goldstein (1983, 1985), Goldstein, Sockol & Sanz (1983), Zavol'skii, Reutov & Ryboushkina (1983) and Ruban (1985) solidified the mechanisms by which long-wavelength free-stream disturbances at a particular frequency are converted to a wavelength commensurate with the boundary-instability wave. From the theoretical, numerical and experimental points of view, the receptivity mechanism of isolated small height roughness is well understood (Gaster 1965; Murdock 1980; Goldstein 1983; Kerschen 1989, 1990; Dietz 1999; Wu 2001; Saric *et al.* 2002). The receptivity mechanism shows that the deviation on the length scale of eigenmodes from a smooth surface can excite TS waves by interacting with free-stream disturbances or acoustic

noise. From a theoretical point of view, Ruban (1984), Goldstein (1985) and Duck, Ruban & Zhikharev (1996) studied the interactions of free-stream disturbances with an isolated steady hump confined within the viscous sublayer of a triple-deck region. Wu (2001) also investigated the interaction of steady distributed wall roughness with either acoustic or vortical free-stream disturbances with the triple-deck theory framework. For distributed roughness, Corke, Sever & Morkovin (1986) further inferred that the faster growth of TS waves on the rough wall was not attributable to the destabilisation effect of roughness, such as an inflectional instability, and claimed that the growth is due to the continual excitation of TS waves on the rough wall by free-stream turbulence.

In contrast, the interaction between TS waves and rapid distortions on the wall also has practical significance for prediction of laminar–turbulent transition (Wu 2001) but has not received so much attention. A rapid distortion refers to the TS waves are modulating over a length scale comparable with, or shorter than, the streamwise wavelength. For smooth distortions, analyses by Smith (1973, 1981), based on triple-deck theory, provided a good understanding of the physics of imperfection on the wall. Numerical solutions of the nonlinear triple-deck equations for the flows over a hump were also obtained by Sykes (1978), Napolitano, Davis & Werle (1979) and Smith & Merkin (1982).

For isolated rapid distortions, when the height of the roughness exceeds a problem-dependent critical value, bypass transition can be triggered without the growth stage of TS waves through a strong inflectional instability mechanism (Savin, Smith & Allen 1999). However small-amplitude roughness, which are located in the viscous sublayer, has a relatively small modification of the streamwise component of the boundary layer base flow profile. Wörner, Rist & Wagner (2003) numerically investigated the influence of two-dimensional humps and steps on the stability characteristics of a two-dimensional laminar boundary layer by direct numerical simulations (DNS). This study indicated that a localised rectangular hump destabilises the laminar boundary layer. In a three-dimensional flat-plate boundary layer flow, disturbances excited by surface three-dimensional roughness also have significant impact on the boundary layer. Considering a spanwise three-dimensional roughness array, there are some experimental and numerical studies of roughness elements on transition. Experimentally, for a flat-plate boundary layer using a spanwise roughness array to excite controlled stationary disturbances, low-speed experiments of White (2002) indicated that roughness induces suboptimal disturbance growth. White & Ergin (2003) investigated how the steady disturbance energy in spatial wavelengths scales with roughness amplitude. Fischer & Choudhari (2004) carried out DNS for various roughness configurations that enable detailed comparisons with the measurements of White & Ergin (2003). Using suitably designed roughness elements placed on the skin to enforce nearly optimal perturbations, Fransson *et al.* (2006) showed that transition is delayed. However, the topic of disturbances induced by three-dimensional roughness elements is beyond the scope of our discussion in this paper.

Whilst studying the acoustic radiation of TS waves being scattered by a localised roughness in a subsonic compressible boundary layer, Wu & Hogg (2006) also analysed the impact of the roughness on transition. They showed that, as the TS wave propagates through and is scattered by the mean-flow distortion induced by the roughness, it acquires a different amplitude downstream. They introduced the concept of a transmission coefficient, defined as the ratio of the TS wave amplitude after being amplified by the local roughness to that of the incident TS wave, to quantify the impact of the roughness on transition. In this study they observed that a

two-dimensional surface hump, independent of shape, may stabilise TS waves, which, as they comment, 'comes as a surprise'. However it was also noted that this was only the case when the hump is 'small' and if it is not then a nonlinear calculation is necessary. Therefore in this paper, our interest is to study, through nonlinear DNS, the behaviour of unstable TS waves when the base flows are distorted by rapidly varying localised imperfections on the wall and to understand whether TS waves are energised or weakened by this type of small roughness. We further investigate the relative magnitude of the strengthening or weakening of the TS wave as compared to a flat plate.

The paper is organised as follows. In § 2 we introduce the governing equation and the fundamental definitions used in this paper. The basic numerical strategies and configurations are provided in § 3. Our results and discussion are then provided in § 4.

2. Problem formulation

The non-dimensional momentum and continuity equations for an unsteady viscous fluid with constant density are defined by

$$\partial_t \boldsymbol{u} + \boldsymbol{u}\cdot\boldsymbol{\nabla}\boldsymbol{u} = -\boldsymbol{\nabla} p + Re^{-1}\nabla^2\boldsymbol{u} \quad \text{with } \boldsymbol{\nabla}\cdot\boldsymbol{u} = 0, \tag{2.1}$$

where $\boldsymbol{u} = (u, v, w)$ denotes the velocity vector normalised by U_∞, p is the kinematic pressure and Re is a Reynolds number defined by LU_∞/ν, where L is the distance from the leading edge to an isolated surface roughness and ν is the kinematic viscosity. The Cartesian coordinates (x, y) are normalised by L. In the flat-plate simulations undertaken, it is assumed that Re is large, so that the base flow can be approximated by the well-known Blasius equation

$$f'''(\eta) + \tfrac{1}{2} f(\eta) f''(\eta) = 0, \tag{2.2}$$

subjected to the boundary conditions

$$f(\eta) = f'(\eta) = 0 \quad \text{at } \eta = 0, \tag{2.3a}$$

$$f' = 1 \quad \text{at } \eta \to \infty, \tag{2.3b}$$

where the prime denotes the derivative with respect to the similarity variable η. Specifically in the above the dimensionless variables are defined as follows:

$$f = \Psi/\sqrt{\nu U_\infty x} \quad \text{and} \quad \eta = y\sqrt{U_\infty/(\nu x)}, \tag{2.4a,b}$$

where Ψ is the stream function. The streamwise and vertical velocity profiles of the Blasius boundary layer can be calculated from the following relationships:

$$U_B = \frac{\partial \Psi}{\partial y} = U_\infty f'(\eta) \quad \text{and} \quad V_B = -\frac{\partial \Psi}{\partial x} = \frac{1}{2}\sqrt{\frac{\nu U_\infty}{x}}(\eta f'(\eta) - f(\eta)). \tag{2.5a,b}$$

In order to determine the behaviour of the TS waves, when the base flow is distorted by a hump or indentation, we solve the following linearised system,

$$\partial_t \tilde{\boldsymbol{u}} + \bar{\boldsymbol{u}}\cdot\boldsymbol{\nabla}\tilde{\boldsymbol{u}} + \tilde{\boldsymbol{u}}\cdot\boldsymbol{\nabla}\bar{\boldsymbol{u}} = -\boldsymbol{\nabla}\tilde{p} + Re^{-1}\nabla^2\tilde{\boldsymbol{u}} \quad \text{with } \boldsymbol{\nabla}\cdot\tilde{\boldsymbol{u}} = 0, \tag{2.6}$$

where $\tilde{\boldsymbol{u}}$ and $\bar{\boldsymbol{u}}$ are the perturbed velocity vector and the base flow velocity vector, respectively, and $\tilde{p}$ is the perturbed kinematic pressure. For a flat-plate boundary layer, $\bar{\boldsymbol{u}}$ is defined by the Blasius flow (U_B, V_B).

Considering the above linearised equations as is typically done for the Orr–Sommerfeld equation, we now non-dimensionalise in the normal manner with respect to the free-stream velocity U_∞ and the displacement thickness of the Blasius boundary layer, δ_*. For convenience, we still use $\bar{\boldsymbol{u}}$ and $\tilde{\boldsymbol{u}}$ to denote the non-dimensional base flow field and the perturbed velocity field. Then, without distortions, under the assumption of streamwise parallel flow in two dimensions, the perturbation assumes the normal form

$$(\tilde{u}, \tilde{v}, \tilde{p}) = (\hat{u}, \hat{v}, \hat{p}) \exp(\mathrm{i}(\alpha x - \omega t)) + \text{c.c.} \tag{2.7}$$

From the linearised Navier–Stokes equations follows the well-known Orr–Sommerfeld (OS) equation for $\hat{v}$,

$$[(-\mathrm{i}\omega + \mathrm{i}\alpha U(y))(\mathcal{D}^2 - \alpha^2) - \mathrm{i}\alpha U''(y) - Re_{\delta_*}^{-1}(\mathcal{D}^2 - \alpha^2)]\hat{v}(y) = 0, \tag{2.8}$$

where Re_{δ^*} is the displacement thickness Reynolds number defined by $U_\infty \delta^*/\nu$ and the boundary conditions are characterised from the fact that the perturbation velocities vanish at the wall $(y = 0)$ and decay to zero in the main stream $(y = \infty)$, and so are given by

$$\hat{v}(y) = \mathcal{D}\hat{v}(y) = 0 \quad \text{at } y = 0, \tag{2.9a}$$

$$\hat{v}(y), \mathcal{D}\hat{v}(y) \to 0 \quad \text{for } y = \infty \ (\mathcal{D} = \partial_y). \tag{2.9b}$$

For a given real ω, the solution of the OS equation consists of a spatial discrete spectrum and a continuous spectrum when y ranges from 0 to ∞. The solution of this mathematical problem for eigenvalues and eigenfunctions is well described in several references (Stuart 1963; Schlichting 1968; Drazin & Reid 1981).

Owing to the distortion of small-scale humps/indentations, the base flows are distorted locally and therefore, as a TS wave approaches the roughness site, it is scattered by the rapid distortion. In order to describe the problem by adopting the scales used in the triple-deck theory as is illustrated in figure 1 (Neiland 1969; Stewartson & Williams 1969; Messiter 1970), we introduce the scales $xRe^{-3/8}$ and $xRe^{-5/8}$. Then, the following scales are defined around the roughness elements:

$$X = (x - x_c)/(x_c Re^{-3/8}) \quad \text{and} \quad Y = y/(x_c Re^{-5/8}), \tag{2.10a,b}$$

where x_c is the centre of the roughness elements.

By the coordinate transformation (2.10), the waves can now be described locally by $\tilde{\boldsymbol{u}}(X, Y, t)$. For an unstable frequency $\omega \in \mathbb{R}^+$, the TS wave envelope is defined by the absolute maximum amplitude of the TS wave as follows:

$$A^{max}(X) = \max\left\{|\tilde{u}(X, Y, t)| : \forall Y \in [0, \infty), \forall t \in \mathbb{R}^+\right\}. \tag{2.11}$$

The distorted TS wave envelopes for humps/indentations are therefore denoted by

$$A_h^{max}(X) \quad \text{and} \quad A_i^{max}(X), \tag{2.12a,b}$$

where the subscripts h and i refer to hump and indentation, respectively. Similarly for a flat-plate boundary layer, let $A_f^{max}(x)$ denote the absolute maximum amplitude of the TS wave.

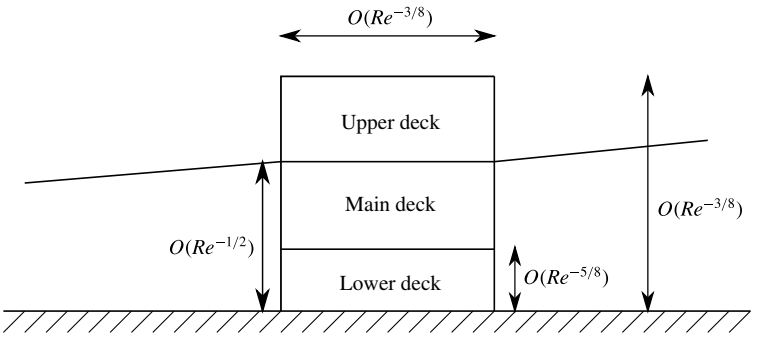

FIGURE 1. Schematic figure of the triple-deck structure.

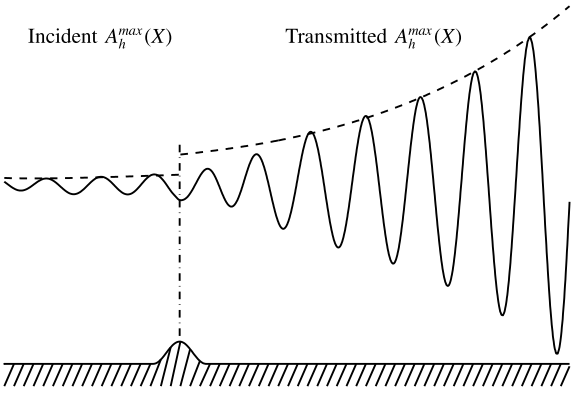

FIGURE 2. Schematic illustration of transmitted TS waves when a base flow is distorted by a hump.

In order to quantify the difference between $A_f^{max}(x)$ and $A_{h,i}^{max}(X)$, the following quantities are introduced:

$$\mathcal{T}_{h,i}(X) = A_{h,i}^{max}(X)/A_f^{max}(X). \tag{2.13}$$

Following the asymptotic theory, for $X \gg 1$ and when the Blasius boundary layer recovers after being disturbed by a distortion, according to linear theory, $\mathcal{T}_{h,i}(X)$ should be constant. Under these conditions, the value then becomes the so-called transmission coefficient $\mathcal{T}_{h,i}(\infty)$, which was introduced in Wu & Hogg (2006). The value of $\mathcal{T}_{h,i}(\infty)$ can be defined by the ratio of right limit and left limit of $A_h^{max}(X)$ at the discontinuity point as is illustrated in figure 2.

To investigate the $\hat{h}$ dependence of $\mathcal{T}_{h,i}(X)$, it is convenient to introduce the closely related quantity $\mathcal{T}_{h,i}^*(x)$:

$$\mathcal{T}_{h,i}^*(x) = \mathcal{T}_{h,i}(x) - 1. \tag{2.14}$$

Similarly, in order to investigate the shear stress distribution around local surface imperfections, we introduce the shear stress notation

$$\tau_f(X), \quad \tau_h(X), \quad \tau_i(X), \tag{2.15a–c}$$

where the subscripts f, h and i again refer to flat plate, hump and indentation, respectively. We note that shear is evaluated using the strain rate $\partial\tilde{u}/\partial y$ in a direction

normal to the flat plate in both the theoretical and computational evaluations. The following quantities are also useful in presenting the $\hat{h}$ dependence of the shear stress around the hump and indentation as compared to the flat-plate conditions:

$$\tau_h^*(X) = \tau_h(X)/\tau_f(X) - 1, \quad \tau_i^*(X) = \tau_i(X)/\tau_f(X) - 1. \tag{2.16a,b}$$

The values $\tau_{h,i}^*$ can be interpreted as the deviation from one of the shear stresses of the hump/indentation relative to the flat-plate shear stress.

In the subsequent calculations, the rescaled width ($\hat{d}$) and height ($\hat{h}$) are defined by

$$\hat{d} = d/(x_c Re^{-3/8}) \quad \text{and} \quad \hat{h} = h/(x_c Re^{-5/8}). \tag{2.17a,b}$$

3. Direct numerical simulations

In this work the base flows were generated by means of DNS of the two-dimensional nonlinear Navier–Stokes equations (NSEs), where we used initial and boundary conditions calculated through the Blasius boundary layer equations. The base flows were subsequently used in the two-dimensional linearised Navier–Stokes equation (LNSEs) to calculate the TS wave behaviour. Both the NSEs and the LNSEs make use of a spectral element discretisation in space (for additional details the interested reader can refer to Karniadaks & Sherwin (2005)). The geometry of the humps/indentations was described by using high-order curved elements. In particular both the flow and the geometry were described by seventh-order polynomial basis functions. Note that, for the base flow generation, the inlet and outlet positions are located sufficiently far from the localised roughness location in order to allow the base flow to recover the Blasius profile. In addition, in the simulations of the LNSEs, the OS eigenfunction is prescribed as inlet boundary conditions while an absorption region (Israeli & Orszag 1981) was used to damp the TS waves at the outlet.

3.1. *Base flows and physical configuration*

We consider the boundary layer with a small localised imperfection over a flat plate and define the local Reynolds number, $Re_{\delta_*} = (U_\infty \delta_*)/\nu$, in terms of the free-stream velocity U_∞ and the local Blasius boundary layer displacement thickness, δ_*. The initial conditions for solving NSEs are set by the Blasius solution. In order to guarantee steady-state convergence of (2.1), we used the tolerance

$$\|\partial_t u^n\|_0 / \|u^n\|_0 < 10^{-7}, \tag{3.1}$$

where $\|\cdot\|_0$ is the standard L^2 norm. Figure 3 illustrates the evolutions of the convergent criteria given by (3.1) for the generation of the base flows distorted by the humps. Figure 4 shows the velocity components and their derivatives along the normal direction at different downstream positions for $\hat{h} = 1.2$, once a convergent solution is obtained. It is observed that, numerically, the streamwise Blasius component is recovered quickly. However, the vertical Blasius component recovery needs a longer downstream distance.

Using the simulated data, we are interested in exploring the behaviour of transmitted TS waves. Therefore, we investigated the characteristics of the base flows around localised imperfections which are located in the unstable regime according to the neutral stability diagram of the flat-plate boundary layer for $Re_{x_c} = 440\,000$.

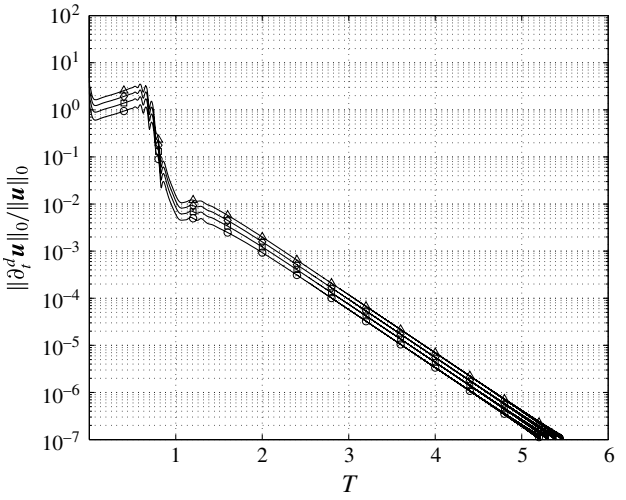

FIGURE 3. Convergent criteria $\|\partial_t^d \boldsymbol{u}\|_0/\|\boldsymbol{u}\|_0$ evolutions for the generation of base flows distorted by humps, where ∂_t^d denotes the discrete time derivative operator. Height/depth $\hat{h} = 0.6$ (○), 0.8 (□), 1 (◇), 1.2 (△) and width $\hat{d} = 1$. The non-dimensional quantity T is defined as t/T_c (where T_c is a typical time scale).

To guarantee domain size independence, we located the inlet and the outlet sufficiently far from the roughness position ($X < -45$ and $X > 45$ for upstream and downstream, respectively) so that the Blasius profiles were consistently recovered. In the wall normal direction, we adopted a domain where the Blasius similarity variable was $\eta = y/\delta \in [0, 70]$.

Through the above configuration, the numerically determined base flows were observed to be independent of the computational domain size. This was also corroborated by ensuring that, when we specified the Blasius profile at the inlet, the Blasius profile was recovered before the outlet.

In order to ensure that solid walls were sufficiently smooth and to avoid the slow decay of an exponentially shaped function, the shape $y = f(x)$ of the roughness is defined as

$$f(x) = \begin{cases} 0, & x - x_c < -d/2, \\ \pm\dfrac{h}{2}\left(1 + \cos\left(\dfrac{2\pi(x - x_c)}{d}\right)\right), & x - x_c \in [-d/2, d/2], \\ 0, & x - x_c > d/2, \end{cases} \tag{3.2}$$

where d and h are the streamwise width and wall-normal scales, receptively. Therefore, $+h$ and $-h$ denote the height (and depth) of humps and indentations, respectively.

Figure 5(a) depicts the computational domain used for the hump simulations. As mentioned previously, the hump was constructed using a seventh-order polynomial representation of the geometry. The background coarse mesh employed for specific hump simulations is shown in figure 5(b), while figure 5(c) illustrates the solution points within each element of the mesh. We used a polynomial of order seven within each element of the mesh in order to achieve a consistent approximation between the geometry and the equations.

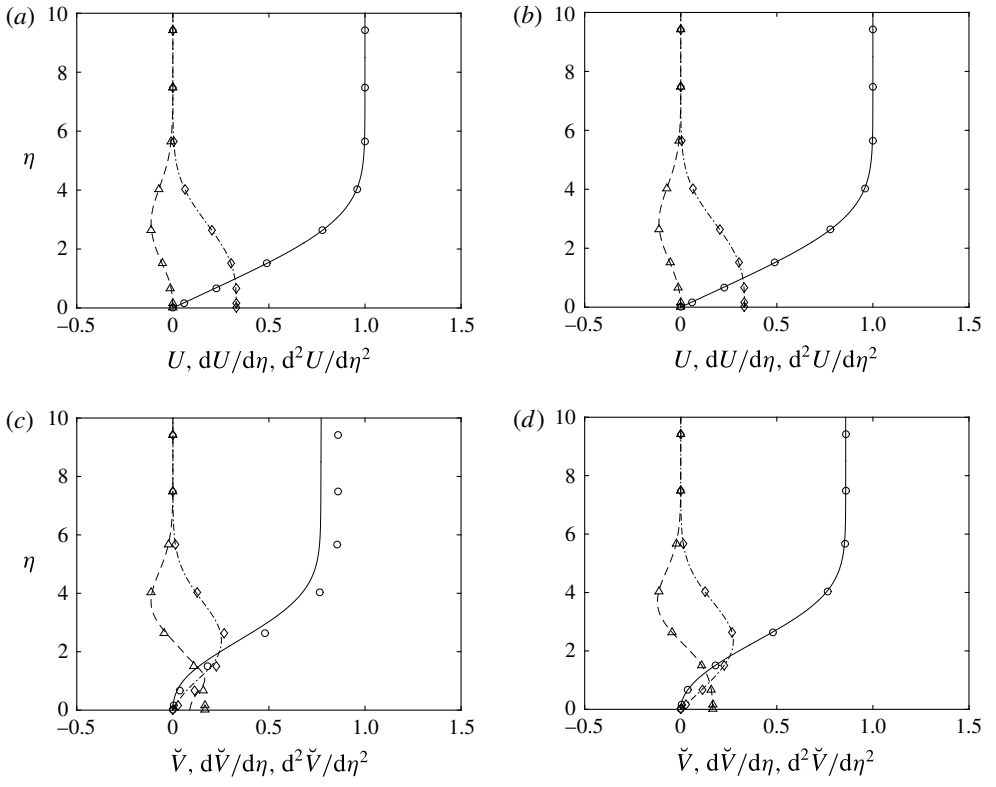

FIGURE 4. Comparisons of streamwise (*a*,*b*) and normal (*c*,*d*) velocities and their derivatives with respect to η: (*a*,*c*) at $X = 10$; (*b*,*d*) at $X = 30$. The solutions calculated by DNS: ——, U in (*a*,*b*) and $\breve{V}$ in (*c*,*d*); — —, $\mathrm{d}U/\eta$ in (*a*,*b*) and $\mathrm{d}\breve{V}/\eta$ in (*c*,*d*); — · —, $\mathrm{d}^2U/\mathrm{d}\eta^2$ in (*a*,*b*) and $\mathrm{d}^2\breve{V}/\mathrm{d}\eta^2$ in (*c*,*d*). The reference quantities obtained from Blasius solution: ○, U_B in (*a*,*b*) and $\breve{V}_B$ in (*c*,*d*); ◇, $\mathrm{d}U_B/\mathrm{d}\eta$ in (*a*,*b*) and $\mathrm{d}\breve{V}_B/\mathrm{d}\eta$ in (*c*,*d*); △, $\mathrm{d}^2U_B/\mathrm{d}\eta^2$ in (*a*,*b*) and $\mathrm{d}^2\breve{V}_B/\mathrm{d}\eta^2$ in (*c*,*d*). Here, $U(\eta) = \bar{u}(\eta\delta)/U_\infty$, $\delta = x/\sqrt{Re_x}$, $\breve{V}_B(\eta) = \eta f'(\eta) - f(\eta)$ (see (2.5)), $\breve{V}(\eta) = 2\bar{v}(\eta\delta)\sqrt{Re_x}/U_\infty$, $\delta = x/\sqrt{Re_x}$ and $\hat{h} = 1.2$.

The mesh configuration and the polynomial order adopted for each simulation were based on *P*-refinement independence where the L^2 relative error of the shear stress along the solid wall was of order $O(10^{-5})$ in all cases.

3.2. *Inflow perturbations for the LNSEs*

It is well known that, under a parallel flow assumption, the non-zero solutions of the eigenvalue problem for the OS equation with $\omega \neq 0$ are usually TS waves.

In our computations, because the position where we wish to enforce an incoming TS wave when solving the LNSEs is within the domain of the base flow calculation, the LNSEs are solved in a smaller domain than that used for the base flow simulations. In the smaller domains, only the inlet position was changed to guarantee that the inlet displacement Reynolds number is in the unstable regime of the neutral stability diagram (or at the neutral position of the lower branch of the neutral curve). So, when the inlet displacement Reynolds number Re_{δ_*} lies in the unstable regime for a given real frequency ω, the normal velocity at the inlet is defined by the most unstable

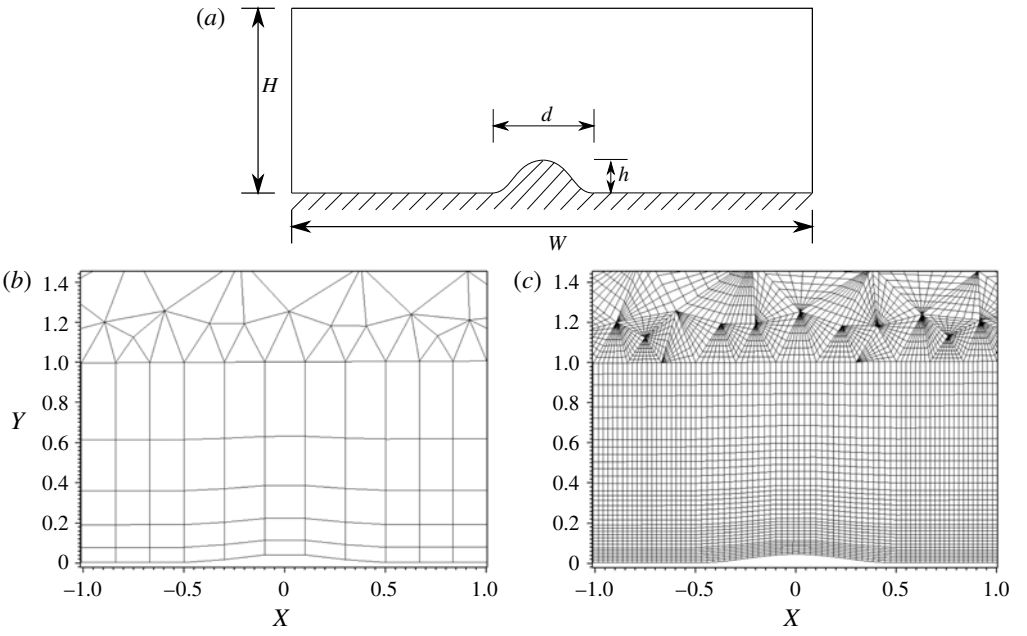

FIGURE 5. Schematic illustration of the computational domain and the mesh around a hump: (*a*) the computational domain with a smooth hump on the lower boundary, where h and d denote the height and width of the hump, respectively; (*b*) low-order background mesh around the hump; and (*c*) high-order body-fitted mesh around the hump ($\hat{h}=1,\ \hat{d}=1$).

eigenfunction of the discrete spectrum. With the aid of the divergence-free condition, we can obtain the streamwise component $\tilde{u}(y)$ corresponding to (2.7). Mathematically, the inlet boundary condition is formulated as

$$\tilde{\boldsymbol{u}} = \epsilon\,\mathrm{Re}[(-\mathrm{i}\alpha^{-1}\hat{v}'(y),\,\hat{v}(y))\exp(-\mathrm{i}\omega t)], \tag{3.3}$$

where ϵ can be an arbitrary non-zero constant. In our simulations, the dimensionless frequency $\mathcal{F}$ is defined by

$$\mathcal{F} = \frac{\omega}{Re_{\delta_*}} \times 10^6. \tag{3.4}$$

4. Results

The behaviour of transmitted TS waves is determined by a distorted base flow. As the length scale of the distorted base flow is comparable with the characteristic wavelength of the TS wave, the concept of local stability analysis is not tenable. The physical process by which the roughness influences the disturbance is through scattering. The wave downstream of the roughness will be referred to as the transmitted wave. Typically, the shear stress distribution of a given base flow around a small localised imperfection on the wall has a significant impact on the behaviour of TS waves. Classically, triple-deck theory is used to describe locally distorted base flows (see figure 1 for a schematic triple-deck structure). In this section, we firstly review the lower-deck structure and the corresponding linearised approximation.

Next, we discuss the shear stress distribution in terms of the linearised lower-deck theory. Finally, we discuss the applicability of the linearised theory in formulating the transmission coefficient. The transmission behaviour is subsequently evaluated numerically for various configurations.

4.1. *Linearised lower deck*

The classical triple-deck theory (Neiland 1969; Stewartson & Williams 1969; Messiter 1970) is based upon the small parameter ε; the asymptotic dimensionless thickness is defined by

$$\varepsilon = Re^{-1/2}. \tag{4.1}$$

The streamwise length scale of the roughness (or other forms of variation) is of order $O(\varepsilon^{-3/4})$; we introduce

$$X = \varepsilon^{-3/4}(x - x_c)/x_c. \tag{4.2}$$

In each deck, the following normal direction variables are adopted:

$$\text{upper deck} \quad Y^* = \varepsilon^{-3/4} y, \tag{4.3a}$$

$$\text{main deck} \quad Y = \varepsilon^{-1} y, \tag{4.3b}$$

$$\text{lower deck} \quad \hat{Y} = \varepsilon^{-5/4} y. \tag{4.3c}$$

The triple-deck structure is illustrated in figure 1 (the asymptotic expansions in each deck are given in appendix A).

We denote by $U_B(Y)$ the non-perturbed Blasius velocity profile of the boundary layer at $x = x_c$ and its slope at the wall is defined as

$$\lambda = \left.\frac{\mathrm{d}U_B(Y)}{\mathrm{d}Y}\right|_{Y=0}. \tag{4.4}$$

Without loss of generality, let λ be equal to 1 and the final system of the lower deck is independent of the base flow. This can be achieved by introducing the following rescaled quantities:

$$X := \lambda^{5/4} X, \quad \hat{Y} := \lambda^{3/4} \hat{Y}, \tag{4.5a,b}$$

and

$$u = \lambda^{-1/4}\varepsilon^{1/4}\hat{u}_1 + \cdots, \quad v = \lambda^{-3/4}\varepsilon^{3/4}\hat{v}_1 + \cdots, \quad p = \lambda^{-1/2}\varepsilon^{1/2}\hat{p}_1 + \cdots. \tag{4.6a–c}$$

It is assumed that, locally, the hump/indentation has the profile (Smith 1973)

$$y/x_c = \varepsilon^{5/4}\hat{h}F(X), \tag{4.7}$$

where $\hat{h}$ is initially of order one and the function F is such that $\hat{h}F(X)$ is of order one or less. Consider now the case $\hat{h} \ll 1$. Equations (A 7) can be linearised about the undisturbed boundary layer profile by introducing the following expansions:

$$\left.\begin{array}{c} \hat{u}_1 = \hat{Z} + \hat{h}\breve{u}_1 + O(\hat{h}^2), \quad \hat{v}_1 = \hat{h}\breve{v}_1 + O(\hat{h}^2), \quad \hat{p}_1 = \hat{h}\breve{p} + O(\hat{h}^2), \\ A = \hat{h}\breve{A}_1 + O(\hat{h}^2), \end{array}\right\} \tag{4.8}$$

where $\hat{Z} = \hat{h}F(X)$. For subsonic flows, Smith (1973) gave the following for the streamwise pressure gradient and shear stress solution to the linearised lower deck equations:

$$\frac{\mathrm{d}\hat{p}}{\mathrm{d}X} = \frac{\hat{h}\theta^3}{2\pi}\int_{-\infty}^{\infty} F(X-t)\alpha(t)\,\mathrm{d}t, \tag{4.9a}$$

$$\tau = 1 + \hat{h}\breve{u}_{1,Z}(X,0) = 1 - \frac{3\hat{h}\mathrm{Ai}(0)\theta^{4/3}}{2\pi}\int_{-\infty}^{\infty} F(X-t)\beta(t)\,\mathrm{d}t, \tag{4.9b}$$

where $\mathrm{Ai}(X)$ denotes the Airy function, $\theta = [-3\mathrm{Ai}'(0)]^{3/4}$, and $\alpha(t)$ and $\beta(t)$ are two special functions of t (Smith 1973), which are given in appendix B.

For the fixed hump/indentation shape $F(X)$, (4.9*a*) and (4.9*b*) are independent of the integrals on their right-hand sides. Therefore, the scaling relations

$$\frac{\mathrm{d}\hat{p}}{\mathrm{d}X} \sim \hat{h}, \quad \tau - 1 \sim \hat{h}, \tag{4.10a,b}$$

hold for a hump, and changing the sign of $\hat{h}$, the above relations also hold for indentations.

4.2. *Behaviour of shear stress and pressure distributions*

To investigate the influence of hump/indentation on the behaviour of transmitted TS waves and assess the validity of the transmission coefficient $\mathcal{T}_{h,i}(\infty)$ estimated by the linearised lower-deck theory, we calculated the shear stress and pressure distributions around the roughness position. The quantities corresponding to the shear stress and pressure distributions are obtained by numerically solving the NSEs. The numerical problem is chosen so that the Reynolds number at the centre of the distortion is $Re_{x_c} = 440\,000$, which corresponds to a displacement Reynolds number of $Re_{\delta_*} = 1140.1$. This Reynolds number was chosen since it is possible to capture unstable TS waves at a frequency similar to that studied by Wu & Hogg (2006). In all investigations, $\hat{d} = 1$ means that the hump (or indentation) is restricted to $|X| < 1/2$ and $d/\delta_{99} = 1.03$. Figure 6(*a*,*b*) shows the deviation from one of the vertical shear stress relative to the flat-plate conditions $\tau_h^*(X)$ and $\tau_i^*(X)$ for different values of $\hat{h}$ on humps and indentations, respectively. For reference, when $Re_{x_c} = 440\,000$, $\hat{h} = 0.6$ and 1.2 correspond to $h/\delta_{99} = 2.4\,\%$ and $4.8\,\%$, where δ_{99} is based on the Blasius boundary flat-plate thickness at x_c. We recall that, following (4.10), the relations

$$\tau_h^*(X) \sim \hat{h}, \quad \tau_i^*(X) \sim -\hat{h} \tag{4.11a,b}$$

are expected to hold true. Therefore, the ratios $\tau_h^*(X)/\hat{h}$ and $\tau_i^*(X)/\hat{h}$ are expected to collapse to a single curve, which is illustrated in figure 6(*c*,*d*). It is evident that the collapse is relatively good. However, around maximum/minimum values of the hump/indentation, the deviations of $\tau_{h,i}^*(X)/\hat{h}$ from the theoretical predictions do show notable discrepancies. For the relatively small parameters considered, we observe a maximum deviation of 16.4 % in the hump and 19.3 % in the indentation. We note that the region, just downstream of the surface hump/indentation do not collapse within the plotting range.

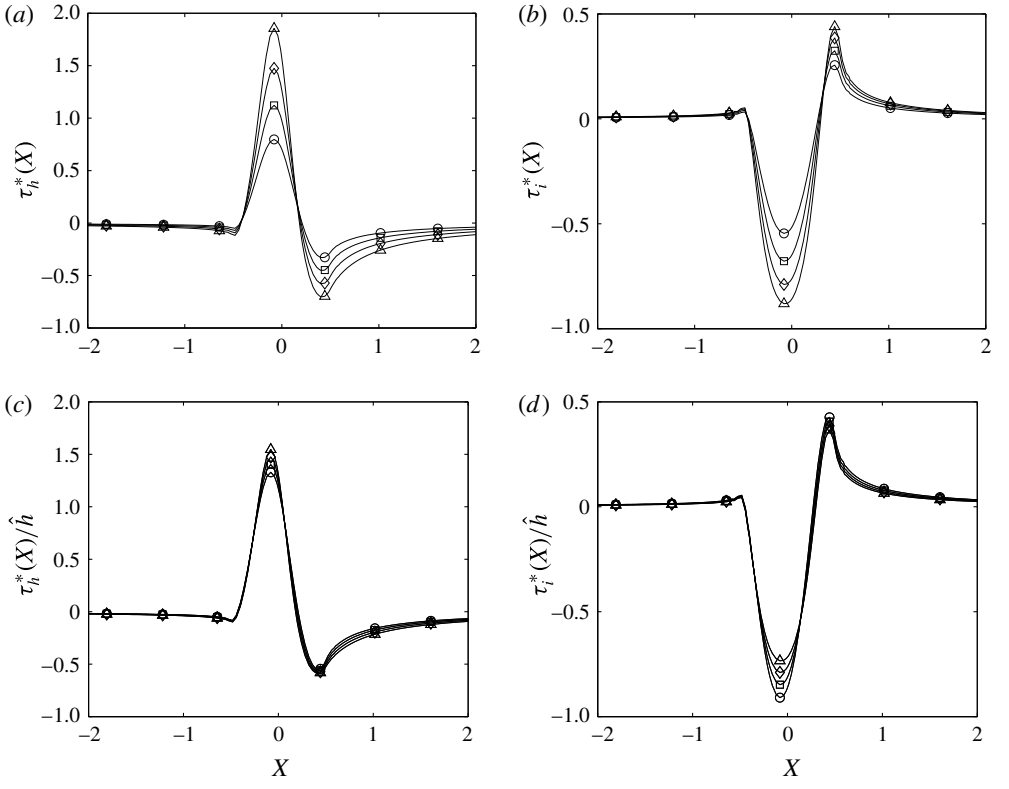

FIGURE 6. Distributions of the relative shear stress deviation, $\tau_{\#}^*(X)$ and $\tau_{\#}^*(X)/\hat{h}$ (the notation '#' denotes h or i) around small-scale humps and indentations: (*a*) $\tau_h^*(X)$ distributions around humps; (*b*) $\tau_i^*(X)$ distributions around indentations; (*c*) $\tau_h^*(X)/\hat{h}$ distributions around humps; and (*d*) $\tau_i^*(X)/\hat{h}$ distributions around indentations. Here $Re_{\delta_*} = 1140.1$; height/depth $\hat{h} = 0.6$ (○), 0.8 (□), 1 (◇), 1.2 (△) and width $\hat{d} = 1$.

Figure 7 shows the pressure distributions $\hat{p}_{1,h}(X)$ and $\hat{p}_{1,i}(X)$ around humps and indentations. Considering (4.10), the pressure gradient $\mathrm{d}\hat{p}_{1,h}(X)/\mathrm{d}X$ and $\mathrm{d}\hat{p}_{1,i}(X)/\mathrm{d}X$ normalised by $\hat{h}$ also should collapse. From figure 7, we observe that, although overall the curves collapse reasonably well, there exists some significant deviation from the prediction at the minimum and maximum values, particularly in the indentation case.

In figure 8 we show some comparisons between a hump and an indentation for the same $\hat{h}$. Following the linearised lower-deck theory, with a small value of $\hat{h}$ we expect $\tau_h^*(X)/\hat{h}$ and $-\tau_i^*(X)/\hat{h}$ to have the same profile, and similarly this should also hold for $\mathrm{d}\hat{p}_{1,h}(X)/\mathrm{d}X$ and $-\mathrm{d}\hat{p}_{1,i}(X)/\mathrm{d}X$. In figure 8(*a*,*b*) when $\hat{h} = 0.6$ we observe that the normalised shear stress and pressure gradient do not overlap. However in figure 8(*c*,*d*), when we reduce the size of the distortion to $\hat{h} = 0.1$ and 0.05 (corresponding to $h/\delta_{99} = 0.4\,\%$ and $0.2\,\%$, where δ_{99} is the flat boundary layer thickness at the roughness centre position), a relatively good agreement between the hump and indentation is observed and is in reasonable agreement with the linearised theory (Smith 1973). Nevertheless this highlights the very small height required to achieve this level of agreement. We further note that in reducing the roughness height to $\hat{h} = 0.1$ and 0.05 we have not changed the width of the hump/indentation,

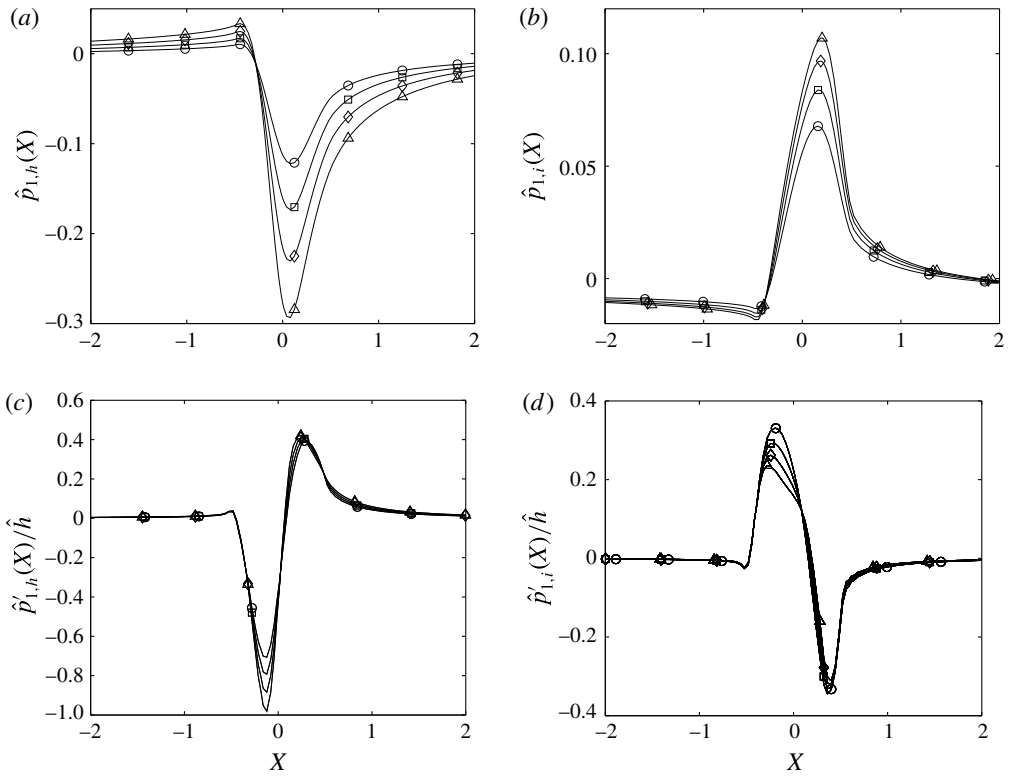

FIGURE 7. Distributions of pressure and pressure gradient normalised by $\hat{h}$ around small humps and indentations: (*a*) pressure distribution around humps; (*b*) pressure distribution around indentations; (*c*) normalised $\mathrm{d}P(X)/\mathrm{d}X$ distribution around humps; and (*d*) normalised $\mathrm{d}P(x)/\mathrm{d}X$ distribution around indentations. Here $Re_{\delta_*} = 1140.1$; height/depth $\hat{h} = 0.6$ (○), 0.8 (□), 1 (◇), 1.2 (△) and width $\hat{d} = 1$.

which was kept at $\hat{d} = 1$, making the slope of the hump/indentation smaller in the streamwise direction. For the cases of relatively large humps/indentations $\hat{h} > 0.1$, there exists a deviation of at least 11.5 % between the numerical results from the linearised theoretical results.

It is clear from figure 8(*a*,*b*) that the deviation between the hump and indentation is not simply due to a constant scaling factor. However, it is worth mentioning that, for a wider hump/indentation scale ($d \sim \lambda_{TS}$), a very accurate prediction has been observed through a similar analysis with the linearised triple-deck theory. This implies that, for a fixed $\hat{h}$, the accuracy of the linearised theory is dependent on $\hat{d}$. That is to say, even though $\hat{h}$ is very small, the theoretical precision is dependent on the ratio $\hat{h}/\hat{d}$, which captures the streamwise slope of the distortion.

4.3. *Behaviour of transmitted TS waves*

We now turn our attention to the behaviour of the transmitted TS waves. To formulate the influence of humps and indentations on the TS waves, the transmission coefficient, defined analytically by Wu & Hogg (2006), was numerically evaluated to quantify

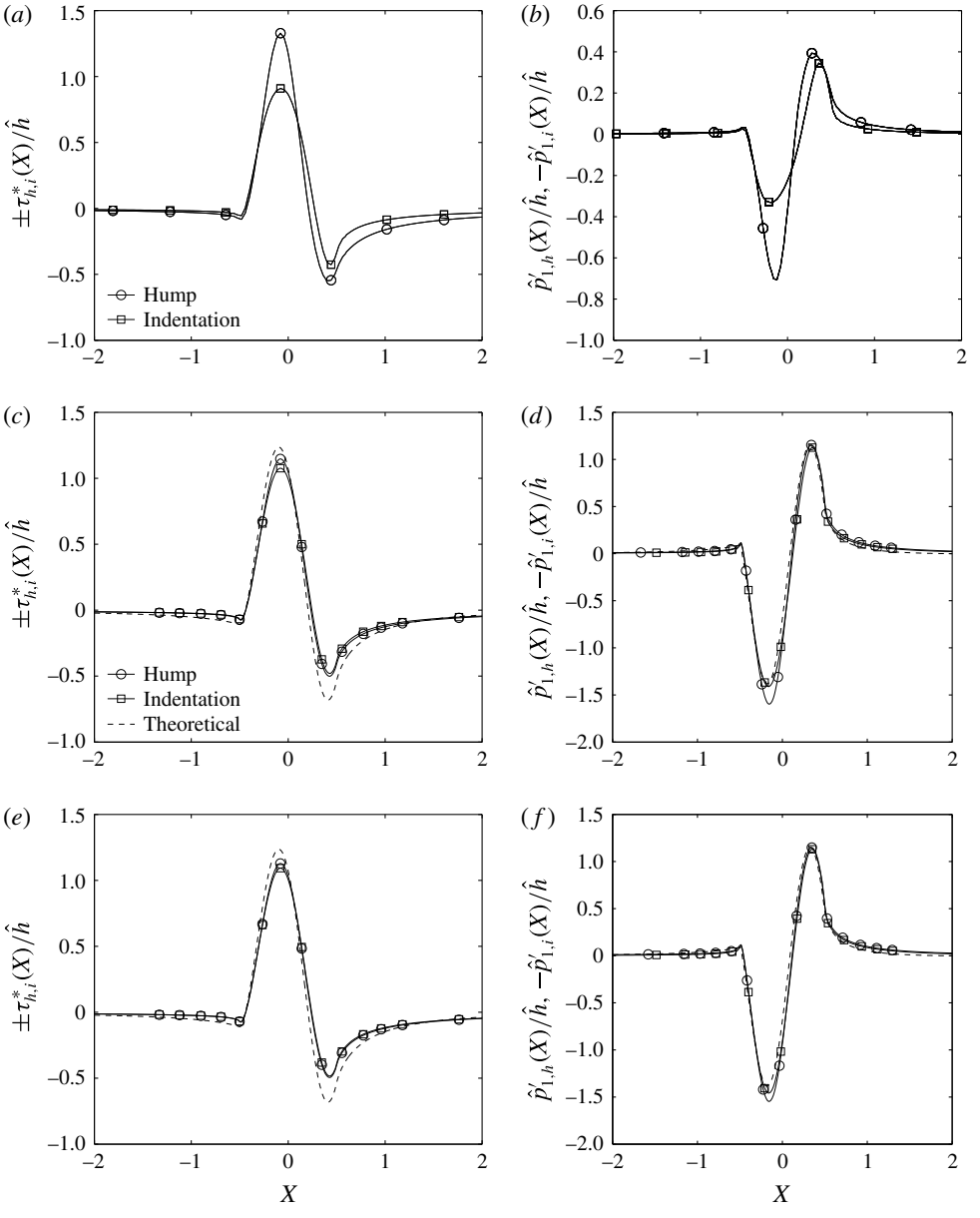

FIGURE 8. Normalised shear stress $\tau^*_{\#}(X)/\hat{h}$ and pressure gradient $\mathrm{d}P(X)/\mathrm{d}X$ distributions normalised by $\hat{h}$ around small-scale humps and indentations: (*a*) $\tau^*_{\#}(X)/\hat{h}$ distributions for $\hat{h}=0.6$; (*b*) normalised $\mathrm{d}P(X)/\mathrm{d}X$ distributions for $\hat{h}=0.6$; (*c*) $\tau^*_{\#}(X)/\hat{h}$ distributions for $\hat{h}=0.1$; (*d*) normalised $\mathrm{d}P(X)/\mathrm{d}X$ distributions for $\hat{h}=0.1$; (*e*) $\tau^*_{\#}(X)/\hat{h}$ distributions for $\hat{h}=0.05$; and (*f*) normalised $\mathrm{d}P(X)/\mathrm{d}X$ distributions for $\hat{h}=0.05$. The roughness elements are located at $Re_{\delta_*}=1140.1$. The width $\hat{d}=1$.

the TS wave behaviour. As is illustrated in figure 2, the theoretical definition of the transmission coefficient is introduced

$$\mathscr{T}_r = A_T^{max}(0+)/A_I^{max}(0-), \tag{4.12}$$

and for $\hat{h} \ll 1$, Wu & Hogg (2006) gave the analytic expression

$$\mathscr{T}_r = 1 + \left\{ \frac{(2\pi)^{1/2}\alpha_2}{\alpha_1 \Delta'(\alpha)} (\mathrm{i}\alpha_1\lambda)^{1/3} \int_{\eta_0}^{\infty} K(\eta, \eta_0) \left(2\eta_0 - \frac{4}{3}\eta\right) \mathrm{Ai}'(\eta)\, \mathrm{d}\eta \right\} \varepsilon^{1/4}\hat{h}\hat{F}(0), \tag{4.13}$$

where λ is the local skin friction, and $\hat{F}(k)$ is the Fourier transform of the roughness element shape. Expressions for $K(\eta, \eta_0)$, $\Delta'(\alpha)$, η, η_0 and the other parameters in (4.13) are given in appendix C. In their work, the analytical result of (4.12) was obtained using a triple-deck framework adopting a linear dependence on $\hat{h}$ for a fixed $\hat{F}(0)$. Expression (4.12) therefore indicates that the area that the distortion encompasses rather than its shape is relevant, and that the gain or reduction of the transmitted TS wave amplitude is proportional to $S \equiv \hat{h}\hat{F}(0)$, which is the (rescaled) area enclosed by the roughness contour. It should be pointed out that the derivation $\mathscr{T}_r - 1$ is of order $O(\varepsilon^{1/4}\hat{h})$, much smaller than the expected order $O(\hat{h})$. This is because the leading-order contribution of scattering turns out to be identically zero, leading to a degeneracy of the linear mechanism with respect to $\hat{h}$. That is to say, if the weak nonlinearity of the base flow distortion is considered, $\mathscr{T}_r$ includes a quadratic term of $\hat{h}$ and, with a small parameter ε, $\mathscr{T}_r$ is dominated by this quadratic term. The $O(\varepsilon^{1/4}\hat{h})$ effect was taken into account by extending the triple-deck analysis to the second order.

For sufficiently small but positive $\hat{h}$, a further interesting implication of (4.12) is that $|\mathscr{T}_r| < 1$ and so a hump can stabilise the incoming TS waves whereas an indentation can destabilise the incoming TS waves (Wu & Hogg 2006). That humps and indentations have opposite effects is a simple consequence of linearity and is expected, provided $\hat{h}$ is sufficiently small.

Figure 9 shows the behaviour of transmitted TS waves using the nonlinear base flows and the linearised calculations for the scattering of the TS waves. In this figure and for the subsequent calculation of the numerical transmission coefficient, we evaluate the transmission coefficient at a fixed X location by determining the peak magnitude of the TS wave undergoing a distortion divided by the magnitude of the TS wave at the same X location over a flat plate. Therefore, as $X \to \infty$ we expect to recover the theoretical transmission coefficient. In figure 9(*a*), within a range close to the distortions $X \in [-6, 6]$, it can be seen that the TS waves can indeed be stabilised ($\mathcal{T}_h(X) < 1$) downstream of small-amplitude humps consistently with the theory. However, further downstream, as is shown in figure 9(*b*), this is not the case, and the overall influence of the hump is to destabilise the TS waves. Figure 9(*c*,*d*) demonstrates that, for the case of indentations, and for values of $\hat{h}$ presented, the TS waves are always destabilised. For the current configurations, we therefore observe that humps and indentations have a similar destabilisation influence on TS waves. We further observe that, for the same $\hat{h}$, the hump transmission coefficient, $\mathcal{T}_h(\infty)$, is greater than the indentation transmission coefficient, $\mathcal{T}_i(\infty)$ ($X \gg 1$).

As already mentioned, we anticipate from (4.12) that $\mathscr{T}_r$ is dependent on $\hat{h}$ for a fixed roughness profile $\hat{F}(X)$ and so $\mathcal{T}_h^*(X)/\hat{h}$ and $\mathcal{T}_i^*(X)/\hat{h}$ should collapse around the distortions. Therefore in figure 10 we consider the numerical transmission coefficient scaled by $\hat{h}$ and observe an approximate collapse within a localised range $X \in [-1, 1]$. However, beyond this range, the distorted TS waves do not appear to collapse. This is due to the $\varepsilon^{1/4}$ scaling in (4.13). Clearly, owing to the distortion of the hump/indentation, the boundary layer is changed and, locally, the TS waves do not

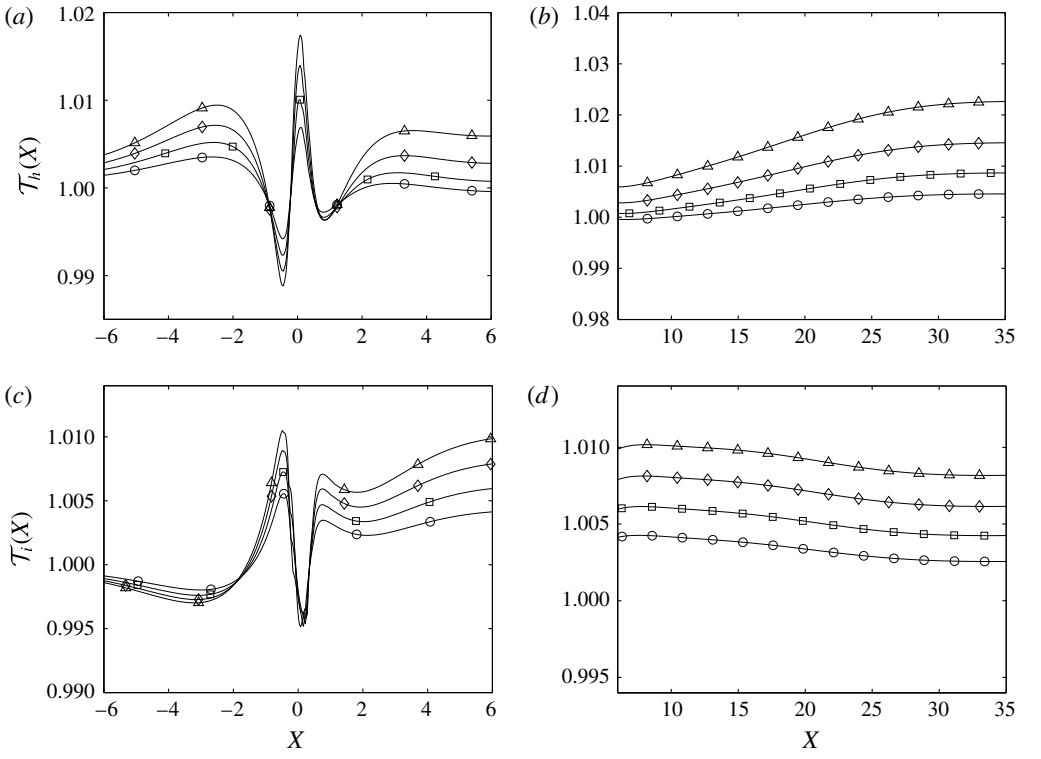

FIGURE 9. Functions $\mathcal{T}_{\#}(X)$ around humps and indentations (the notation '#' denotes h or i): (*a*) $\mathcal{T}_h(X)$ for $X \in [-6, 6]$; (*b*) $\mathcal{T}_h(X)$ for further downstream; (*c*) $\mathcal{T}_i(X)$ for $X \in [-6, 6]$; and (*d*) $\mathcal{T}_i(X)$ for further downstream. Here $Re_{\delta_*} = 1140.1$ and $\mathcal{F} = 55.10$; $\hat{h} = 0.6$ (○), 0.8 (□), 1 (◇), 1.2 (△) and width $\hat{d} = 1$.

maintain similar growth and decay rates to those of TS waves in a flat-plate Blasius boundary layer. Wu & Hogg (2006) put forward the model that the effect of a localised roughness element is to instantly 'boost' the amplitude of the TS waves. Nevertheless, this numerical study indicates that the amplification arises over quite a significant streamwise scale in the case of these relatively short streamwise scale distortions.

In figure 11, we provide a comparison between a hump and an indentation with the same value of $\hat{h} = 1$ ($h/\delta_{99} = 3.9\,\%$). From figure 11(*a*), it is clear that, when $X \to \infty$, the influence of humps on TS waves is greater than that of indentations. In addition, in figure 11(*b*), where we show the deviation of the transmission coefficient from a unit value and have reversed the sign in front of $\mathcal{T}_i^*(X)$, we observe a similar qualitative behaviour. As a comparison, for a much smaller $\hat{h} = 0.1$ ($h/\delta_{99} = 0.39\,\%$), the same conclusion can be drawn from figure 11(*c*,*d*) that the asymptotic theory does become valid at this smaller amplitude. Upstream of the hump and indentation, the profiles of $\mathcal{T}_h^*(X)/\hat{h}$ and $-\mathcal{T}_i^*(X)/\hat{h}$ have already collapsed very well. Although the hump and indentation subsequently demonstrate different magnitudes of destabilisation of the TS waves downstream of the hump and indentation, the overall pattern is much more similar than for the $\hat{h} = 1$ case. Clearly this supports the trend that, as $\hat{h} \to 0$,

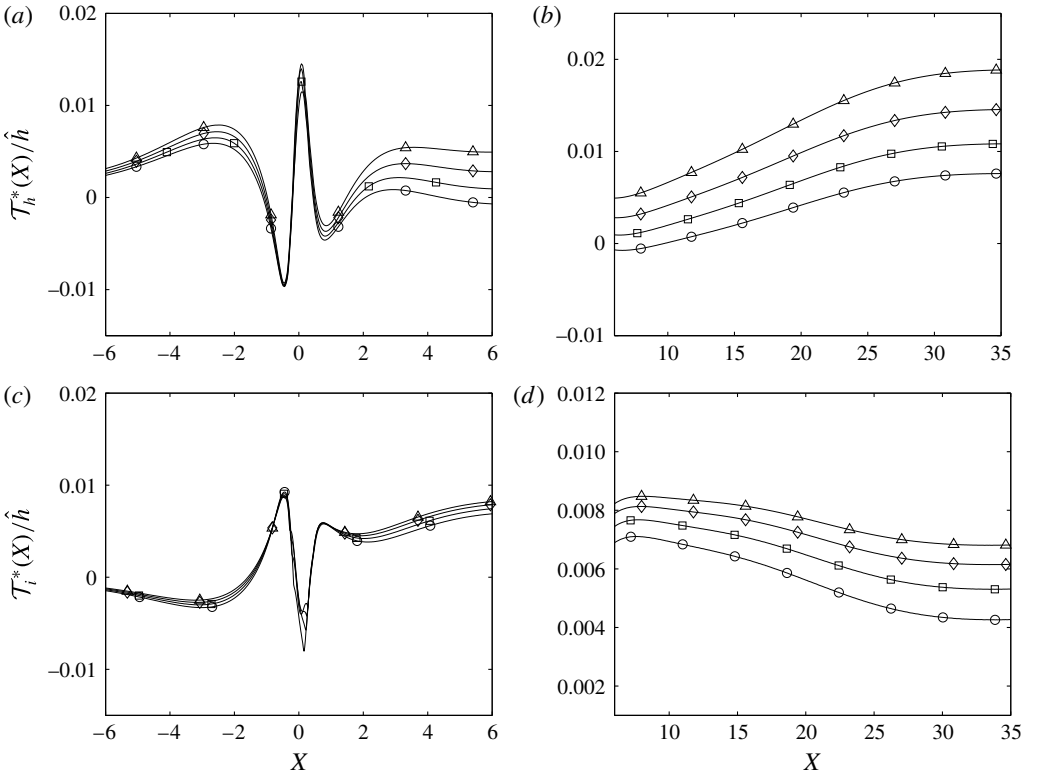

FIGURE 10. Functions $\mathcal{T}_{\#}^*(X)/\hat{h}$ around humps and indentations (the notation '#' denotes h or i): (*a*) $\mathcal{T}_h^*(X)/\hat{h}$ for $X \in [-6, 6]$; (*b*) $\mathcal{T}_h^*(X)/\hat{h}$ for $X \in [6, 35]$; (*c*) $\mathcal{T}_i^*(X)/\hat{h}$ for $X \in [-6, 6]$; and (*d*) $\mathcal{T}_i^*(X)/\hat{h}$ for $X \in [6, 35]$. Here $Re_{\delta_*} = 1140.1$ and $\mathcal{F} = 55.10$; $\hat{h} = 0.6$ (○), 0.8 (□), 1 (◇), 1.2 (△) and width $\hat{d} = 1$.

$\mathcal{T}_h^*(X)/\hat{h}$ and $-\mathcal{T}_i^*(X)/\hat{h}$ will indeed collapse and the numerical results recover the linear theory.

4.3.1. *Effect of height and width of distortion on the transmission coefficient*

For the range $0.05 < \hat{h} < 1.4$ ($0.4\,\% < h/\delta_{99} < 5.5\,\%$) currently considered with $\hat{d} = 1$, we have only observed a transmission coefficient of maximum 2 %. For this numerical study we have fixed our value of Reynolds number to $Re_{x_c} = 440\,000$ and so the TS wave grows spatially with a growth rate of $\alpha_i = -0.011$ at $Re_{x_c} = 878\,036$. If we assume that transition arises downstream of the distortion when the TS wave magnitude A_0 has grown approximately $\ln(A_T/A_0) = 3$, then the transition would arise at $X = 130$ (approximately $130\delta_{99}$) downstream of the initial position of the TS (and where we place the distortion). Under this set of assumptions, if $\mathcal{T}_{\#}^*(\infty)$ has values 1 %, 10 % and 100 %, these will lead to a change of 0.36 %, 3.37 % and 24.0 % of the distance from the distortion to the point of transition. Clearly, from a practical point of view, we would like to understand what features lead to a larger transmission coefficient.

The main geometric features which could lead to a change in transmission coefficient are a change in $\hat{h}$ and $\hat{d}$. A non-exhaustive investigation can be summarised

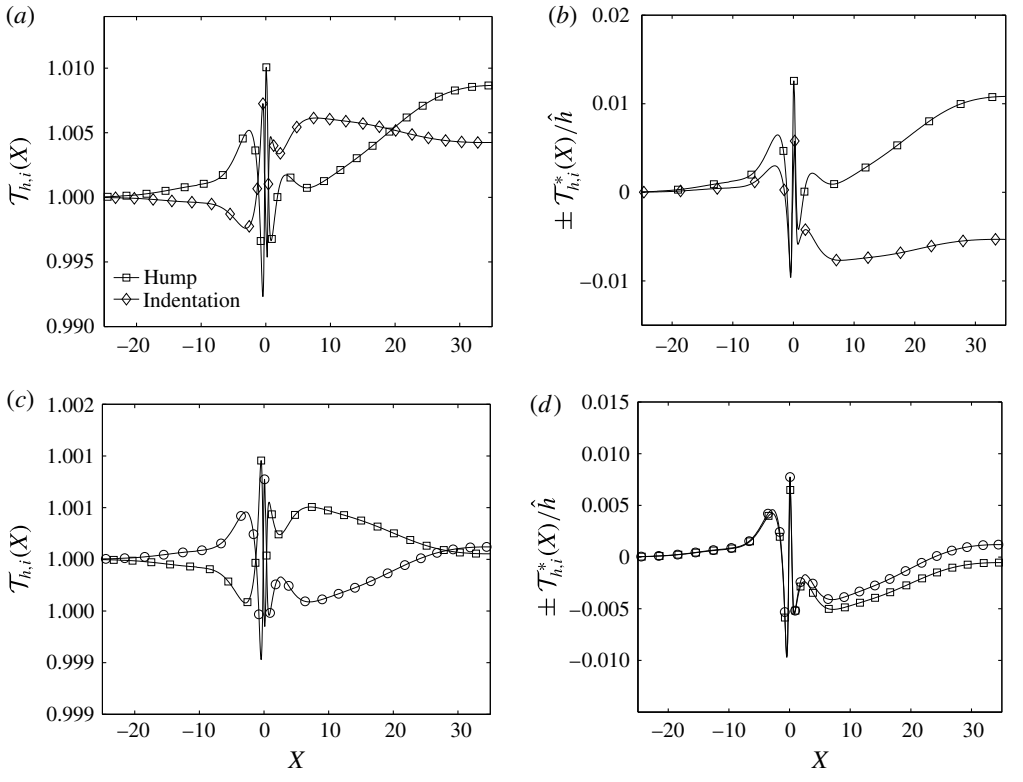

FIGURE 11. Comparisons of $\mathcal{T}_{h,i}(X)$ and $\mathcal{T}^*_{h,i}(X)/\hat{h}$: (*a*) $\mathcal{T}_{h,i}(X)$ for $\hat{h}=1$; (*b*) $\mathcal{T}^*_h(X)/\hat{h}$ and $-\mathcal{T}^*_i(X)/\hat{h}$ for $\hat{h}=1$; (*c*) $\mathcal{T}_{h,i}(X)$ for $\hat{h}=0.1$; and (*d*) $\mathcal{T}^*_h(X)/\hat{h}$ and $-\mathcal{T}^*_i(X)/\hat{h}$ for $\hat{h}=0.1$. The roughness elements are located at $Re_{\delta_*}=1140.1$. Here $\mathcal{F}=55.10$ and the width $\hat{d}=1$.

in the data in figure 12. In this figure we show the variation of the transmission coefficient as a function of $\hat{h}$ at $\hat{d}=1$ as well as reduced set of data points for $\hat{d}=\lambda_{TS}$, $\lambda_{TS}/2$ and $\lambda_{TS}/3$.

If we assume that there exists a relation between $\mathcal{T}_{\#}(\infty)$, $\hat{F}(0)$ and $\hat{h}$ of the form

$$\mathcal{T}_{\#}(\infty)=1+\Lambda\hat{h}^{\alpha}\hat{F}(0), \tag{4.14}$$

where Λ is a constant, an empirical fit to the exponent α can be determined from the log–log plotting of the data in figure 12. We observe that, for very small values of $\hat{h}$, where we observed that the transmission coefficient did tend to follow the linear theory, a value of approximately $\alpha=1.5$ is observed. When we continue to increase $\hat{h}$ so that the flow around the hump and indentation are no longer similar ($0.1<\hat{h}<1.4$), but the flow remains attached, we observe a potential fit of $\alpha\approx 2$. For even larger values of $\hat{h}$ ($h/\delta_{99}=7.2\,\%$), the flow becomes detached, and at a value of $\hat{h}=5$ ($h/\delta_{99}=20\,\%$) we observe a transmission coefficient of 350 % for the hump. For distortions of $\hat{d}=1$, we clearly only see significant transmission coefficients when the height has become sufficiently large and in this case the flow has separated from the distortion. Further, when $\mathcal{T}^*_h(X)$ and $\mathcal{T}^*_i(X)$ are rescaled by

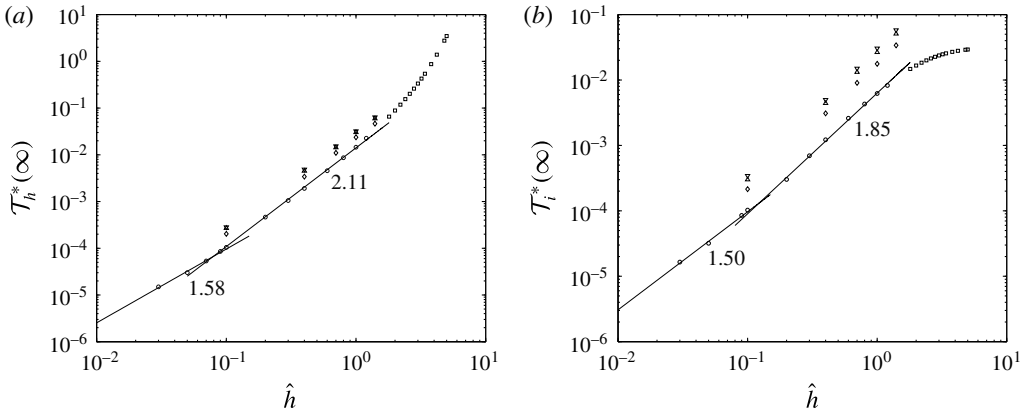

FIGURE 12. Transmission coefficient $\mathcal{T}_{\#}$ (the notation '#' denotes h or i): (a) for humps; and (b) for indentations. Symbols denotes cases where the flow is attached (○) and cases where the flow is separated (□) when $\hat{d}=1$. Other symbols denote attached flow when $\hat{d}=\lambda_{TS}/3$ (◇), $\hat{d}=\lambda_{TS}/2$ (△) and $\hat{d}=\lambda_{TS}$ (▽).

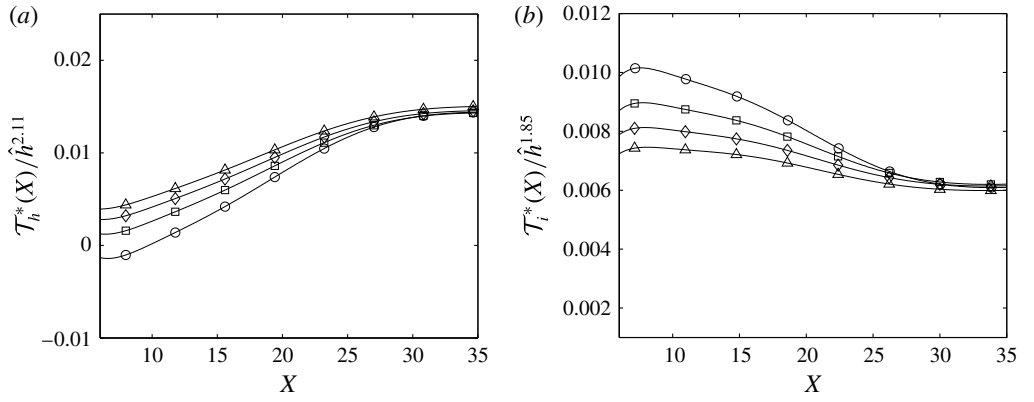

FIGURE 13. Functions $\mathcal{T}_{\#}^*(X)/\hat{h}$ around humps and indentations (the notation '#' denotes h or i): (a) $\mathcal{T}_h^*(X)/\hat{h}^{2.11}$ for $X\in[6,35]$; and (b) $\mathcal{T}_i^*(X)/\hat{h}^{1.85}$ for $X\in[6,35]$. Here $Re_{\delta_*}=1140.1$ and $\mathcal{F}=55.10$; $\hat{h}=0.6$ (○), 0.8 (□), 1 (◇), 1.2 (△) and width $\hat{d}=1$.

$\hat{h}^{2.11}$ and $\hat{h}^{1.85}$, respectively, we observe an approximate collapse further downstream for both $\mathcal{T}_h^*(X)/\hat{h}^{2.11}$ and $\mathcal{T}_i^*(X)/\hat{h}^{1.85}$ in figure 13.

However, when the distortion has a width that is comparable with the TS wavelength, large transmission coefficients are also possible. This factor is encapsulated by the $\hat{F}(0)$ term in (4.12) and (4.14), which we recall represents the Fourier transform of the roughness element. The data for $\hat{d}=\lambda_{TS},\ \lambda_{TS}/2,\ \lambda_{TS}/3$ as opposed to the values for when $\hat{d}=1=\lambda_{TS}/11.3$ lead to far larger transmission coefficients, nearly an order of magnitude higher. We also observe that, in the range of data considered, the slope of $\alpha\approx 2$ seems to remain. If the analysis of Wu & Hogg (2006) is extended to include the weak nonlinearity of the base flow distortion, then

$$\mathcal{T}_r = 1+\Lambda_1\varepsilon^{1/4}\hat{h}+\Lambda_2\hat{h}^2, \tag{4.15}$$

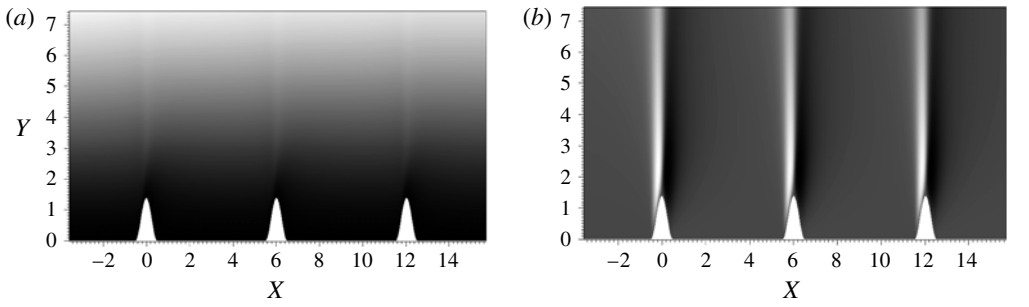

FIGURE 14. Base flow for $\hat{h} = 1.4$: (*a*) horizontal velocity; and (*b*) vertical velocity.

where $\Lambda_2 \sim O(1)$. The result indicates that the linear approximation requires a more stringent condition $\hat{h} \ll \varepsilon^{1/4}$ rather than $\hat{h} \ll 1$. Therefore, when $\varepsilon^{1/4} \ll \hat{h} \ll 1$, there is a degeneracy of the linear mechanism, where the transmission coefficient can be seen to behave primarily as a quadratic function of $\hat{h}$.

4.3.2. *Effect of multiple isolated roughness elements on the TS transmission coefficient*

Individually, when $\hat{d} = 1$ we have observed that the effect of a single isolated small-scale localised distortion on the TS waves is small. Therefore, we consider the effect of multiple isolated roughness elements. Since multiple isolated humps have a similar destabilisation effect on the TS waves as multiple isolated indentations, we consider only the cases of three isolated humps located at $Re_{\delta_*} = 1140.17$, 1166.07 and 1191.40, as is illustrated in figure 14. The three humps are equally spaced and the distance between two adjacent humps is equal to six times the upper-deck scale defined at $Re_{\delta_*} = 1140.17$ or approximately $6\delta_{99}$. The width and height of these three humps are kept the same, which are also defined by the local scales of the first hump located at $Re_{\delta_*} = 1140.17$. For the first hump, the width scale $\hat{d}$ is fixed equal to 1 and the height scale considered includes $\hat{h} = 0.6$, 0.8, 1.0, 1.2 and 1.4. For all cases, there is no separated flow; and the base flow, shear stress and pressure gradients were similar to the isolated cases and are not shown.

The base flow for $\hat{h} = 1.4$ is illustrated in figure 14. Figure 15 shows the profiles of the numerical transmission coefficient for the series of three humps. From figure 15(*a*), we can observe that higher $\hat{h}$ values give rise to a relatively large amplification of the TS waves. When $\hat{h} = 1.4$ ($h/\delta_{99} = 5.5\,\%$), the amplification of the corresponding TS wave is approximately 10 %. In figure 15(*b*), we provide a comparison between multiple humps and a single hump when $\hat{h} = 0.8$ and we observe that the amplification of the TS wave by three humps is very close to three times that by a single hump. For the current configuration, there exists a linear relation between the amplification and number of isolated humps. The effect of multiple humps would theoretically be expected to have a multiplicative influence. However, since each hump has a small transmission coefficient, a linearisation of a multiplicative transmission coefficient gives a linear amplification as observed here. We recall from figure 9(*a*) that for $\hat{h} = 0.6$ at a location of $X = 6$ there exists a small region of stabilisation of the TS waves. However, in the case of multiple humps, spaced by six units, the overall effect is still to destabilise the TS waves.

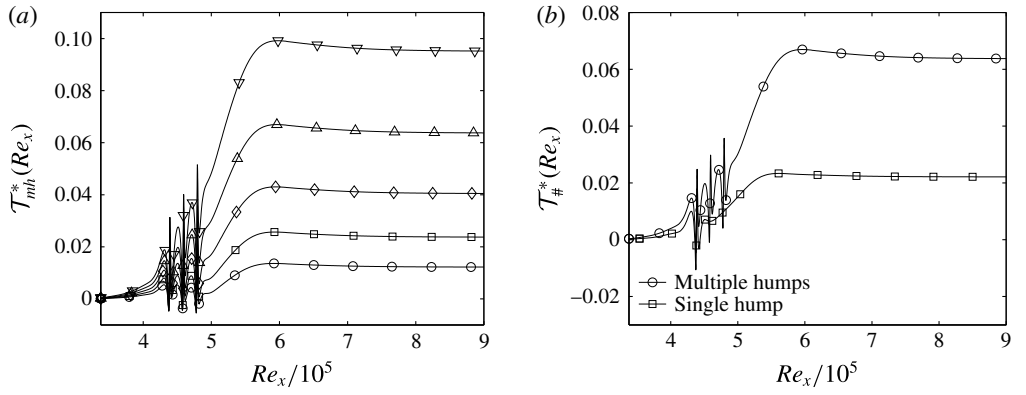

FIGURE 15. Profiles of $\mathcal{T}^*_{mh}(X)$ and $\mathcal{T}^*_{\#}(X)/\hat{h}$: (*a*) profiles of $\tau^*_{mh}(X)$ (height scales $\hat{h}=0.6$ (○), 0.8 (□), 1.0 (◇), 1.2 (△), 1.4 (▽)); and (*b*) profiles of $\tau^*_{mh}(X)/\hat{h}$ for multiple humps (○) and a single hump (□). The width $\hat{d}=1$. The frequency $\mathcal{F}=55.10$. Notation # denotes the single-hump symbol '*h*' or the multiple-hump symbol '*mh*'.

5. Conclusion

In this paper, the spectral element discretisation was employed to numerically analyse the behaviour of the TS waves when the base flow is distorted by a small-scale localised distortion. The base flows were obtained using the fully nonlinear Navier–Stokes equations and the TS wave amplifications was simulated using the linearised Navier–Stokes equations.

For the small-amplitude localised wall distortions considered, humps and indentations both have destabilising effects rather than having opposite effects as expected on the basis of linearity. This indicates that the nonlinearity effect is appreciable despite the relatively small height/depth of humps/indentations. The result is broadly consistent with the degeneracy of the leading-order linear term of the asymptotic analysis.

Notably, for the regime investigated, $0.05 < \hat{h} < 1.4$ ($0.2\,\% < h/\delta_{99} < 5.5\,\%$) at $Re_{\delta_*} = 1140.17$ or $Re_{x_c} = 440\,000$, we observe that, when the transmission coefficient is evaluated downstream of the distortion, both humps and indentations have a destabilising effect on the TS wave, in contrast to the asymptotic theory for smoother distortions, where only indentations were observed to be destabilising in the vicinity of the distortion. The localised distortions considered in this study lead to a significant deviation of the flow from the Blasius flat-plate profile, which is consistent with the deviation of the numerical results from the linearised asymptotic theory. For the parameters studied, an isolated distortion leads to a relatively weak, of the order of 1–2 %, amplification of the TS wave when $\hat{d} = 1$. Increasing the height of the distortion so that the flow locally separates can lead to a much larger transmission coefficient of up to 350 % in the case of a hump of size $\hat{h} = 5$ (corresponding to $h/\delta_{99} = 20\,\%$). In addition, if the hump width is increased to be comparable with the TS wavelength, an increase of nearly one order of magnitude was observed for a fixed hump height.

Finally the introduction of multiple humps when $\hat{d} = 1$ (with a separation of six hump widths) is observed to have an additive effect, allowing the small distortions to obtain more significant amplifications.

Acknowledgements

This research was performed in the Laminar Flow Control Centre (LFC-UK) at Imperial College London. The Centre is supported by EPSRC, Airbus Global Innovations under grant EP/I037946/1. S.J.S. would like to acknowledge support under a Royal Academy of Engineering Research chair. We would also like to acknowledge the helpful input of Gianmarco Mengaldo.

Appendix A. Interaction described by the triple-deck theory

The asymptotic expansions in each deck are given as follows.

(1) Upper deck:

$$\left.\begin{aligned} u &= 1 + \varepsilon^{1/2} u_1^*(X, Y^*) + \cdots, \\ v &= \varepsilon^{1/2} v_1^*(X, Y^*) + \cdots, \\ p &= \varepsilon^{1/2} p_1^*(X, Y^*) + \cdots. \end{aligned}\right\} \tag{A 1}$$

The equations are

$$\frac{\partial u_1^*}{\partial X} + \frac{\partial v_1^*}{\partial Y^*} = 0, \tag{A 2a}$$

$$\frac{\partial u_1^*}{\partial X} = -\frac{\partial p_1^*}{\partial X}, \tag{A 2b}$$

$$\frac{\partial V_1^*}{\partial X} = -\frac{\partial p_1^*}{\partial Y^*}. \tag{A 2c}$$

(2) Main deck:

$$\left.\begin{aligned} u &= U_B + \varepsilon^{1/4} u_1(X, Y^*) + \cdots, \\ v &= \varepsilon^{1/2} v_1(X, Y^*) + \cdots, \\ p &= \varepsilon^{1/2} p_1(X, Y^*) + \cdots. \end{aligned}\right\} \tag{A 3}$$

The equations are

$$\frac{\partial u_1}{\partial X} + \frac{\partial v_1}{\partial Y} = 0, \tag{A 4a}$$

$$U_B \frac{\partial u_1}{\partial X} + u_1 \frac{\partial U_0}{\partial Y} = 0, \tag{A 4b}$$

$$\frac{\partial P_1}{\partial Y} = 0. \tag{A 4c}$$

The solution in the main deck is

$$u_1 = A(X) U_B'(Y) \quad \text{with } U_B'(Y) = \frac{\mathrm{d}U_B}{\mathrm{d}Y}, \tag{A 5a}$$

$$v_1 = -A(X) U_B(Y) \quad \text{with } A'(X) = \frac{\mathrm{d}A}{\mathrm{d}X}, \tag{A 5b}$$

where the function $A(X)$ is called a displacement function, which can be determined such that $A \to 0$ as $X \to -\infty$.

(3) Lower deck:

$$\left.\begin{aligned} u &= \varepsilon^{1/4}\hat{u}_1(X,\hat{Y})+\cdots,\\ v &= \varepsilon^{3/4}\hat{v}_1(X,\hat{Y})+\cdots,\\ p &= \varepsilon^{1/2}\hat{p}_1(X,\hat{Y})+\cdots. \end{aligned}\right\} \tag{A 6}$$

The equations are

$$\frac{\partial \hat{u}_1}{\partial X}+\frac{\partial \hat{v}_1}{\partial \hat{Y}}=0, \tag{A 7a}$$

$$\hat{u}_1\frac{\partial \hat{u}_1}{\partial X}+\hat{v}_1\frac{\partial \hat{u}_1}{\partial \hat{Y}}=-\frac{\partial \hat{p}_1}{\partial X}+\frac{\partial^2 \hat{u}_1}{\partial \hat{Y}^2}, \tag{A 7b}$$

$$\frac{\partial \hat{p}_1}{\partial \hat{Y}}=0. \tag{A 7c}$$

Asymptotically, to order $\varepsilon^{1/4}$, we obtain

$$\lim_{\hat{Y}\to\infty}(\hat{u}_1-\lambda\hat{Y})=\lambda A(X). \tag{A 8}$$

To order $\varepsilon^{1/2}$, we have

$$v_1^*(X,0)=\lim_{Y\to 0} v_1(X,Y). \tag{A 9}$$

Considering (A 3) amd $U_B(\infty)=1$, we have

$$v_1^*(X,0)=\frac{\mathrm{d}A}{\mathrm{d}X}. \tag{A 10}$$

For pressure p, to order $\varepsilon^{1/2}$, the asymptotic matching gives

$$p_1(X,0)=\lim_{\hat{Y}\to 0}\hat{p}(X,\hat{Y}), \tag{A 11a}$$

$$p_1^*(X,0)=\lim_{Y\to 0} p_1(X,Y). \tag{A 11b}$$

Because $\dfrac{\partial p_1}{\partial Y}=0$ and $\dfrac{\partial \hat{p}_1}{\partial \hat{Y}}=0$, we have

$$p_1^*(X,0)=p_1(X)=\hat{p}_1(X). \tag{A 12}$$

For subsonic main stream flow,

$$A''(X)=-\frac{1}{\pi}\int_{-\infty}^{\infty}\frac{\hat{p}'(\xi)}{X-\xi}\,\mathrm{d}\xi. \tag{A 13}$$

Appendix B. Definitions of parameters in (4.9)

$$\alpha=\begin{cases}\displaystyle\int_0^\infty \frac{s^2(3^{1/2}s^{4/3}-2)\exp(-\theta s t)\,\mathrm{d}s}{1-3^{1/2}s^{4/3}+s^{8/3}} & (t>0),\\[2ex] \displaystyle 2\int_0^\infty \frac{s^2\exp(\theta s t)\,\mathrm{d}s}{1+s^{8/3}} & (t<0),\end{cases} \tag{B 1a}$$

$$\beta = \begin{cases} \displaystyle\int_0^\infty \frac{s^{5/3}(3^{1/2}s^{4/3} - 1)\exp(-\theta st)\,\mathrm{d}s}{1 - 3^{1/2}s^{4/3} + s^{8/3}} & (t > 0), \\ \displaystyle 2\int_0^\infty \frac{s^{5/3}\exp(\theta st)\,\mathrm{d}s}{1 + s^{8/3}} & (t < 0). \end{cases} \tag{B 1b}$$

Appendix C. Definitions of parameters in (41.3)

The functions $K(\cdot,\cdot)$ and $\Delta(\cdot)$ respectively are defined by

$$K(\eta, \eta_0) = \pi \frac{\mathrm{Ai}'(\eta_0)\mathrm{Gi}(\eta) - \mathrm{Gi}'(\eta_0)\mathrm{Ai}(\eta)}{\mathrm{Ai}'(\eta)}, \tag{C 1}$$

and

$$\Delta(k) = \int_{\eta_0}^\infty \mathrm{Ai}(\zeta)\,\mathrm{d}\zeta + \mathrm{i}\lambda(\mathrm{i}k\lambda)^{2/3}\mathrm{Ai}'(\eta_0)\frac{\bar{k}}{k^3}, \tag{C 2}$$

where Gi and Gi′ are defined in Abramowitz & Stegun (1964, p. 449), and where $\bar{k} = (1 - M^2)^{1/2}|k|$ (M is the Mach number and $M < 1$ for the subsonic flow). In the theory, the TS wave has a wavenumber α and the mean-flow distortion has a continuous Fourier spectrum, which is a continuous function of wavenumber k. In the above, η and η_0 are defined by

$$\eta = (\mathrm{i}\alpha_1\lambda)^{1/3}Y + \eta_0 \quad \text{and} \quad \eta_0 = -\mathrm{i}\hat{\omega}(\mathrm{i}\alpha_1\lambda)^{-2/3}, \tag{C 3a,b}$$

where $\hat{\omega}$ is the rescaled frequency and α_1 in (C.3) and α_2 in (4.13) are from the asymptotic expansion of the wavenumber α (Wu & Hogg 2006):

$$\alpha = \alpha_1 + \varepsilon\alpha_2 + \varepsilon^2\alpha_3 + \cdots. \tag{C 4}$$

REFERENCES

Abramowitz, M. & Stegun, I. A. 1964 *Handbook of Mathematical Functions*. National Bureau of Standards.

Choudhari, M. & Streett, C. L. 1994 Theoretical prediction of boundary-layer receptivity. *AIAA Paper* 94-2223.

Corke, T. C., Sever, A. B. & Morkovin, M. V. 1986 Experiments on transition enhancements by distributed roughness. *Phys. Fluids* **29**, 3199–3213.

Crouch, J. D. 1994 Theoretical studies on the receptivity of boundary layers. *AIAA Paper* 94-2224.

Dietz, A. J. 1999 Local boundary-layer receptivity to a convected free-stream disturbance. *J. Fluid Mech.* **378**, 291–317.

Drazin, P. G. & Reid, W. H. 1981 *Hydrodynamic Stability*. Cambridge University Press.

Duck, P. W., Ruban, A. I. & Zhikharev, C. N. 1996 Generation of Tollmien–Schlichting waves by free-stream turbulence. *J. Fluid Mech.* **312**, 341–371.

Fischer, P. & Choudhari, M. 2004 Numerical simulation of roughness-induced transient growth in a laminar boundary layer. *AIAA Paper* 2004-2539.

Fransson, J. H. M., Talamelli, A., Brandt, L. & Cossu, C. 2006 Delaying transition to turbulence by a passive mechanism. *Phys. Rev. Lett.* **96**, 064501.

Gaster, M. 1965 On the generation of spatially growing waves in a boundary layer. *J. Fluid Mech.* **22**, 433–441.

Gaster, M. 1974 On the effects of boundary-layer growth on flow stability. *J. Fluid Mech.* **66** (3), 465–480.

GOLDSTEIN, M. E. 1983 The evolution of Tollmien–Schlichting waves near a leading edge. *J. Fluid Mech.* **127**, 59–81.

GOLDSTEIN, M. E. 1985 Scattering of acoustic waves into Tollmien–Schlichting waves by small streamwise variations in surface geometry. *J. Fluid Mech.* **154**, 509–529.

GOLDSTEIN, M. E. & HULTGREN, L. S. 1989 Boundary-layer receptivity to long-wave free-stream disturbances. *Annu. Rev. Fluid Mech.* **21**, 137–166.

GOLDSTEIN, M. E., SOCKOL, P. M. & SANZ, J. 1983 The evolution of Tollmien–Schlichting waves near a leading edge. Part 2. Numerical determination of amplitudes. *J. Fluid Mech.* **129**, 443–453.

HALL, P. & SMITH, F. T. 1984 On the effects of nonparallelism, three-dimensionality, and mode interaction in nonlinear boundary-layer stability. *Stud. Appl. Maths* **70**, 91–120.

HEINRICH, R. A., CHOUDHARI, M. & KERSCHEN, E. J. 1988 A comparison of boundary-layer receptivity mechanisms. *AIAA Paper* 88-3758.

ISRAELI, M. & ORSZAG, S. A. 1981 Approximation of radiation boundary conditions. *J. Comput. Phys.* **41**, 115–135.

KACHANOV, Y. S. 1994 Physical mechanisms of laminar-boundary-layer transition. *Annu. Rev. Fluid Mech.* **26**, 4110482.

KACHANOV, Y. S. 2000 Three-dimensional receptivity of boundary layers. *J. Mech. (*B*/Fluids)* **19**, 723–744.

KARNIADAKS, G. E. & SHERWIN, S. J. 2005 *Spectral/HP Element for Computational Fluid Dynamics*. Springer.

KERSCHEN, E. J. 1989 Boundary layer receptivity. *AIAA Paper* 89-1109.

KERSCHEN, E. J. 1990 Boundary layer receptivity theory. *Appl. Mech. Rev.* **43**, S152–S157.

KOZLOV, V. V. & RYZHOV, O. S. 1990 Receptivity of boundary layers: asymptotic theory and experiment. *Proc. R. Soc. Lond.* A **429**, 341–373.

LIN, C. C. 1966 *The Theory of Hydrodynamic Stability*. Cambridge University Press.

MESSITER, A. F. 1970 Boundary-layer flow near the trailing edge of a flat plate. *SIAM J. Appl. Math.* **18**, 241–257.

MORKOVIN, M. V. 1969 The many faces of transition. In *Viscous Drag Reduction* (ed. C. S. Wells), pp. 1–31. Plenum.

MOSTON, J., STEWART, P. A. & COWLEY, S. J. 2000 On the nonlinear growth of two-dimensional Tollmien–Schlichting waves in a flat-plate boundary layer. *J. Fluid Mech.* **425**, 259–300.

MURDOCK, J. W. 1980 The generation of a Tollmien–Schlichting wave by a sound wave. *Proc. R. Soc. Lond.* A **372**, 517–534.

NAPOLITANO, N., DAVIS, R. T. & WERLE, M. J. 1979 A numerical technique for the triple-deck problem. *AIAA* **17** (7), 78–1133.

NEILAND, V. YA. 1969 Theory of laminar boundary layer separation in supersonic flow. *Mekh. Zhid. Gaz.* **4**, 53–57.

NISHIOKA, M. & MORKOVIN, M. V. 1986 Boundary-layer receptivity to unsteady pressure gradients: experiments and overview. *J. Fluid Mech.* **171**, 219–261.

RUBAN, A. I. 1984 On Tollmien–Schlichting wave generation by sound. *Izv. Akad. Nauk SSSR Mekh. Zhidk. Gaza* **5**, 44–52.

RUBAN, A. I. 1985 On Tollmien–Schlichting wave generation by sound. In *Laminar–Turbulent Transition* (ed. V. V. Kozlov), pp. 313–320. Springer.

SARIC, W. S., REED, H. L. & KERSCHEN, E. J. 2002 Boundary-layer receptivity to free-stream disturbances. *Annu. Rev. Fluid Mech.* **34**, 251–276.

SAVIN, D. J., SMITH, F. T. & ALLEN, T. 1999 Transition of free disturbances in inflectional flow over an isolated surface roughness. *Proc. R. Soc. Lond.* A **455**, 491–541.

SCHLICHTING, H. 1968 *Boundary-Layer Theory*. McGraw-Hill.

SCHUBAUER, G. B. & SKRAMSTAD, H. K. 1948 Laminar-boundary-layer oscillations and transition on a flat plat. *NASA TR*-909.

SMITH, F. T. 1973 Laminar flow over a small hump on a flat plate. *J. Fluid Mech.* **57**, 803–824.

SMITH, F. T. 1979*a* Nonlinear stability of boundary layers for disturbances of various sizes. *Proc. R. Soc. Lond.* A **368**, 573–589.

SMITH, F. T. 1979*b* On the non-parallel flow stability of the Blasius boundary layer. *Proc. R. Soc. Lond.* A **366**, 91–109.

SMITH, F. T. 1981 On boundary-layer flow past two-dimensional obstacles. *J. Fluid Mech.* **113**, 123–152.

SMITH, F. T. & BURGGRAF, O. R. 1985 On the development of large-sized short-scaled disturbances in boundary layers. *Proc. R. Soc. Lond.* A **399**, 25–55.

SMITH, F. T. & MERKIN, J. H. 1982 Triple-deck solutions for subsonic flow past humps, steps, concave or convex corners and wedged trailing edges. *Comput. Fluids* **10** (1), 7–25.

STEWARTSON, K. & WILLIAMS, P. G. 1969 Self-induced separation. *Proc R. Soc. Lond.* A **312** (312), 181–206.

STUART, J. T. 1963 Hydrodynamic stability. In *Laminar Boundary Layer* (ed. L. Rosenhead), pp. 492–579. Oxford University Press.

SYKES, R. I. 1978 Stratification effects in boundary-layer flow over hills. *Proc. R. Soc. Lond.* A **361** (1705), 225–243.

WHITE, E. B. 2002 Transient growth of stationary disturbances in a flat plate boundary layer. *Phys. Fluids* **14** (12), 4429–4439.

WHITE, E. B. & ERGIN, F. G. 2003 Receptivity and transient growth of roughness-induced disturbances. In *33rd AIAA Fluid Dynamics Conference and Exhibit, Orlando, FL.* AIAA 2003-4243.

WLEZIEN, R. W. 1994 Measurement of acoustic receptivity. *AIAA Paper* 94-2221.

WÖRNER, A., RIST, U. & WAGNER, S. 2003 Humps/steps influence on stability characteristics of two-dimensional laminar boundary layer. *AIAA* **41** (2), 192–197.

WU, X. S. 2001 Receptivity of boundary layers with distributed roughness to vortical and acoustic disturbances: a second-order asymptotic theory and comparison with experiments. *J. Fluid Mech.* **431**, 91–133.

WU, X. S. & HOGG, L. W. 2006 Acoustic radiation of Tollmien–Schlichting waves as they undergo rapid distortion. *J. Fluid Mech.* **550**, 307–347.

ZAVOL'SKII, N. A., REUTOV, V. P. & RYBOUSHKINA, G. V. 1983 Excitation of Tollmien–Schlichting waves by acoustic and vortex disturbance scattering in boundary layer on a wavy surface. *J. Appl. Mech. Tech. Phys.* **24** (3), 355–361.

ZHUK, V. I. & RYZHOV, O. S. 1982 On locally inviscid perturbations in a boundary layer with self-induced pressure. *Dokl. Akad. Nauk SSSR* **263** (1), 56–59.